A novel method for tropospheric delay mapping function vertical modeling

Junsheng Ding[1,2,4] · Junping Chen[1,2,3] · Jungang Wang[1,5,6] · Yize Zhang[1]

Abstract

In high-precision space geodetic techniques data processing, the mapping function (MF) is a key factor in mapping the radio waves from the zenith direction down to the signal incoming direction. Existing MF products, either site-wise Vienna Mapping Function (VMF1 and VMF3) or grid-wise VMF1 and VMF3, are only available at the Earth surface. For overhead areas, height correction is always required, which is becoming increasingly important with growing airborne aircraft activity. In this contribution, we introduce a novel method aimed at providing a large number of MFs to the user in a simple and efficient manner, while minimizing the loss of precision. The approach effectively represents the vertical profile of the MFs from the Earth's surface up to altitudes of 14 km. In addition, the new model corrects for height in the assessment using the fifth generation of the European Centre for Medium-Range Weather Forecasts ReAnalysis (ERA5) ray tracing calculations for a global $5° \times 5°$ grid with 54 layers in the vertical direction, a total of 8 azimuths in the plane, and 7 elevation angles, for each day in 2021. Specifically, for both polynomial and exponential model of order 2 and 3, the relative residuals are < 0.3% for the hydrostatic delay MF coefficient a_h, and < 1% for the wet delay MF coefficient a_w. The precision of the new model on the Earth's surface is evaluated using site-wise VMF1 and VMF3 GNSS (Global Navigation Satellite System) products from Technische Universität Wien. The root mean square error of slant hydrostatic delay and slant wet delay at a 3° elevation angle is approximately 4–5 cm and 2–5 cm, respectively.

Keywords European Centre for Medium-Range Weather Forecasts (ECMWF) ReAnalysis 5 (ERA5) · Tropospheric delay · Mapping functions (MF) · Vertical modeling · Ray tracing

1 Introduction

Radio waves are delayed and bent as they pass through the neutral atmosphere due to interaction with gas molecules. The resulting measurement error is called tropospheric delay (Vey et al. 2006; Boisits et al. 2020). One of the most accurate ways of obtaining tropospheric delay is ray tracing through numerical weather models (NWMs) (Landskron and Böhm 2018; Niell 2000; Ding et al. 2023). As the position of the satellite changes rapidly, ray tracing is challenging to compute for every radio wave observation. To quickly obtain the tropospheric delay at any elevation angle, also known as the slant tropospheric delay (STD), it is customary to calculate the tropospheric delay in the zenith direction (ZTD) and then multiply it by the mapping function (MF).

In GNSS meteorology, the accuracy of estimates for precipitable water vapor (PWV) depends on the accuracy of the zenith wet delay (ZWD), i.e., the wet component of the ZTD (Ding et al. 2022). Researchers have developed a variety

✉ Junping Chen
junping@shao.ac.cn

1 Shanghai Astronomical Observatory, Chinese Academy of Sciences, Shanghai 200030, China

2 University of Chinese Academy of Sciences, Beijing 100049, China

3 Shanghai Key Laboratory of Space Navigation and Positioning Techniques, Shanghai Astronomical Observatory, Chinese Academy of Sciences, Shanghai 200030, China

4 Department of Land Surveying and Geo-Informatics, The Hong Kong Polytechnic University, Hong Kong 999077, China

5 Department of Geodesy, GeoForschungsZentrum (GFZ), 14473 Potsdam, Germany

6 Institut für Geodäsie und Geoinformationstechnik, Technische Universität Berlin, 10623 Berlin, Germany

of zenith delay models, including European Geostationary Navigation Overlay Service (EGNOS) model (Penna et al. 2001), Global Pressure and Temperature (GPT) series models (Böhm et al. 2007; Landskron and Böhm 2018), TropGrid series models (Krueger et al. 2004; Schüler 2014), SHAO and SHAtrop series models (Song et al. 2011; Chen et al. 2020), etc. These models generally perform well in evaluation studies (Zhang et al. 2016; Ding and Chen 2020). In contrast, work on MF modeling has been scarce and rather dates back to the end of the last century, such as Chao (1974), Marini (1972), Black and Einser (1984), MTT (Herring 1992), and NMF (Niell 1996). These models are based on standard atmospheric data at sea level or regional sounding data. Others simply provide reference latitudes and seasons in tabular form, such as Black (1978), CfA2.2 (Davis et al. 1985), Foelsche and Kirchengast (2002), UNBabc and UNBab (Guo and Langley 2003), UNB (Urquhart et al. 2014) model, etc.

Niell (2000) proposed the Isobaric Mapping Function (IMF), the first mapping function established by the NWMs ray tracing method, which greatly improved the MF precision. Drawing on this method, Böhm and Schuh (2004) established the Vienna Mapping Function (VMF) and overcome some limitations of the IMF in the wet delay. Böhm et al. (2006) designed the widely used Vienna Mapping Function 1 (VMF1), which has been considered to be the most accurate MF available (Landskron and Böhm 2018). With ensuing adaptations for real-time purposes, the forecast VMF1 model was designed by Böhm et al. (2009). Landskron and Böhm (2018) designed VMF3, which eliminates the deficiencies in the empirical coefficients b and c and in the tuning for a specific elevation angle $3°$ in the VMF1, thus approaching the underlying ray-traced delays more accurately at low elevation angles. By using different NWMs, alternative versions of VMF1 and VMF3, such as UNB-VMF1 (Urquhart and Santos 2011), GFZ-VMF1 (Zus et al. 2015) and GFZ-VMF3, have been derived. In addition, Gegout et al. (2011) introduced the concept of adaptive mapping functions (AMF). The rationale of this approach is to extend the azimuthal dependency of the coefficients through a Fourier series, thereby incorporating a multi-scale azimuthal decomposition. This method is capable of providing GPS range corrections at the measurement level with millimeter precision, even at low elevations. Balidakis et al. (2018) derived a new mapping function GFZ-PT, which describes diurnal and sub-diurnal in addition to long-wavelength variations and provides harmonic functions of ray tracing-derived gradients. Zhang et al. (2021) designed the TMF model assuming an angle between the tropospheric zenith direction and the geometric zenith direction. Zhou et al. (2021) proposed an improved tropospheric mapping function modeling method by adaptively determining the number of coefficients to be estimated in the continuous fraction of the mapping function based on the convergence of a least squares fit.

Overall, numerous zenith delay models and MF models are at hand and provide very accurate tropospheric delays (Kouba 2008, 2009; Yuan et al. 2019; Qiu et al. 2020). However, few of these models consider vertical information of tropospheric delays, which means that most of their applications are limited to the Earth surface. Dousa and Elias (2014) proposed an enhanced model for calculating the tropospheric wet delay by introducing a new parameter for the exponential decay of ZWD. When combined with a reference value, this parameter accurately represents ZWD corrections up to an altitude of 10 km. Li et al. (2018) designed two improved zenith tropospheric delay models, IGGtrop_SH and IGGtrop_rH, based on reanalysis of atmospheric data, which were built based on empirical vertical scaling functions. Validation results showed an average accuracy of 3.86 cm and 3.97 cm, respectively. Balidakis (2019) got hydrostatic and wet mapping factor differences at the orography of the fifth generation of the European Centre for Medium-Range Weather Forecasts (ECMWF) ReAnalysis (ERA5) and virtual orographies 25 m, 100 m, and 500 m above, it is up to ± 0.008 at 500 m height. Zhu et al. (2022) developed the GZTD-P model based on the global ERA5 using a segmentation function to vertically adjust the total zenith delay. The authors verified the accuracy of their model using other atmospheric reanalysis data and sounding station data. Wang et al. (2022) developed a new method to represent NWM-derived tropospheric zenith hydrostatic and wet delays, parameterized by surface values and an additional two or three coefficients, to achieve 1–2 mm precision when reconstructing the delays as NWM-determined delays at any altitude. In contrast to with zenith delay vertical modeling, very little research has been done on the MF vertical modeling. Niell first proposed a linear MF height correction model in 1996, but only for the hydrostatic part (Niell 1996). Qu et al. (2022) identified the shortcoming of constant coefficients in Niell's model and designed a quadratic polynomial to improve the MF coefficients. However, Qu et al. (2022) similarly ignored the wet and restricted the modeling range to altitudes of 0–5 km. In addition, the model was evaluated mainly at the Earth's surface, but not rigorously for the ocean and overhead regions. Yet such evaluation is indispensable today when cm-precision air-borne aircraft activities such as aerial refueling and UAVs traversing jungle obstacle avoidance are on the rise. Another factor to consider is that both linear and quadratic polynomial model are simply approximate mathematical representations of experimental values.

In this contribution, we aim to provide MF height correction models with a global coverage, from the Earth surface to 14 km of altitude, thus comprising the range of most aircraft activities and meteorological events. The models are formulated in a simple and effective way, while minimizing the loss of precision. To simulate the vertical variation of the coefficient a_h and a_w of the tropospheric delay MF, a novel

method is presented, enabling the user to quickly and easily obtain the precise MF. The derivation of the methods is presented in Sect. 2 and the assessment of model performance is presented in Sect. 3. Finally, in Sect. 4, we summarize the work and present the conclusions.

2 Vertical modeling of tropospheric zenith delay mapping functions

In this section, we derive an extensible exponential model of the mapping function coefficients from an exponential function model of the zenith tropospheric delay. We highlight the shortcomings of the Niell height correction model, along with the fact that Niell's linear model was actually an approximation of the exponential model, and then propose an extensible polynomial model as an experimental reference. Finally, a grid point is chosen to demonstrate the new model's performance. Note that this work utilizes the open-source software package RADIATE, developed by the Technische Universität Wien (TU Wien, TUW), to perform ray tracing. The latest VMF3 products are currently generated by this software (Hofmeister 2016; Landskron and Böhm 2018). Program RADIATE uses the Euler radius of curvature, with the gravity acceleration from the more accurate Kraus (2001) formula. More than half of the baselines have a better BLR (Baseline Length Repeatability) at sub-mm difference compared to the NSSA GSFC (http://lacerta.gsfc.nasa.gov/tropodelays) ray tracing (Hofmeister and Böhm 2017).

2.1 Modeling the mapping functions vertical profile

The total delay time experienced by radio waves traveling through the neutral atmosphere at the observation elevation angle ε is usually modeled with the following formula (Davis et al. 1985):

$$\Delta L(\varepsilon) = \text{ZHD} \cdot mf_h(\varepsilon) + \text{ZWD} \cdot mf_w(\varepsilon) \tag{1}$$

Here ZHD and ZWD are delays of the hydrostatic part (ZHD) and wet part respectively, in the zenith direction, and $mf(\varepsilon)$ is the mapping function. The mapping function represents the ratio of the delay on the slant path to the delay in the zenith direction. Its analytical expression draws on three basic coefficients a, b and c:

$$mf(\varepsilon) = \frac{1 + \dfrac{a}{1 + \dfrac{b}{1+c}}}{\sin(\varepsilon) + \dfrac{a}{\sin(\varepsilon) + \dfrac{b}{\sin(\varepsilon)+c}}} \tag{2}$$

In a discrete mapping function, the coefficient a is determined from an NWM; while, the coefficients b and c depend on empirical functions.

Wang et al. (2022) proposed a vertical approximation for zenith delay via the barometric formula, which maintains a precision of 1–2 mm on a global scale. The relationship between zenith delay and height is as follows:

$$\text{ZD}_h = \text{ZD}_0 \cdot e^{\sum_{i=1}^{n}\left(m_i \cdot h^i\right)}, \quad n = 1, 2, 3 \tag{3}$$

where ZD_h and ZD_0 are the zenith delays at geodetic height h and 0, respectively, and m_i are the coefficients of the exponential function. The STD is the product of the zenith delay and the mapping function; while, the STD is not exactly corrected by the zenith delay for height correction, which suggests that the mapping function needs to be corrected. Assume that a function $f(h)$ exists for the following relationship between the mapping functions at height h and 0:

$$mf_h = mf_0 \cdot f(h) \tag{4}$$

To hold Eqs. (1) and (3), $f(h)$ should be an exponential function. Thus, the mapping function at height h and 0 can be expressed by the following formula (note that the exponential coefficients are different from those of Eq. 3):

$$mf_h(\varepsilon) = mf_0(\varepsilon) \cdot e^{\sum_{i=1}^{n}\left(m_i \cdot h^i\right)}, \quad n = 1, 2, 3 \tag{5}$$

The mapping function coefficient a can be derived from Eq. (2):

$$a = -\frac{mf(\varepsilon) \cdot \sin(\varepsilon) - 1}{\dfrac{mf(\varepsilon)}{\sin(\varepsilon) + \dfrac{b}{\sin(\varepsilon)+c}} - \dfrac{1}{1 + \dfrac{b}{1+c}}} \tag{6}$$

Inserting Eqs. (5) into (6), the relationship between the coefficient a_h at height h and the coefficient a_0 at height 0 can be obtained:

$$\frac{1}{a_h} = \frac{1}{a_0} \cdot e^{\sum_{i=1}^{n}\left(m_i \cdot h^i\right)} + \frac{e^{\sum_{i=1}^{n}\left(m_i \cdot h^i\right)} - 1}{1 + \dfrac{b}{1+c}}, \quad n = 1, 2, 3 \tag{7}$$

The term after the plus sign is approximately two orders of magnitude smaller than the term before it. Therefore, we propose the following simplified vertical approximation formula for the coefficient a of the mapping function:

$$a_h \approx a_0 \cdot e^{\sum_{i=1}^{n}\left(m_i \cdot h^i\right)}, \quad n = 1, 2, 3 \tag{8}$$

where a_h and a_0 are mapping function coefficient at height h and 0, respectively (The exponential coefficients are different from those of Eqs. 3, 5, 7, and 8). Note that when the subscripts h and w appear together, h and w refer to hydrostatic and wet, respectively, otherwise h refers to height.

2.2 The height correction of Niell

Niell (1996) proposed an empirical tropospheric delay MF height correction model (called Niell model in this paper), and its coefficients are followed by VMF1 (Böhm et al. 2006) and its successor VMF3 (Landskron and Böhm 2018). In VMF1 and VMF3, the versions with height correction are vmf1_ht and vmf3_ht respectively. The mapping function after height correction is as follows:

$$mf_h(\varepsilon) = mf_0(\varepsilon) + \left(\frac{1}{\sin \varepsilon} - \frac{1 + \frac{a_{ht}}{1 + \frac{b_{ht}}{1 + c_{ht}}}}{\sin \varepsilon + \frac{a_{ht}}{\sin \varepsilon + \frac{b_{ht}}{\sin \varepsilon + c_{ht}}}} \right) \times \frac{h}{1000}$$

(9)

where the constants $a_{ht} = 2.53 \times 10^{-5}$, $b_{ht} = 5.49 \times 10^{-3}$ and $c_{ht} = 1.14 \times 10^{-3}$ define the correction. These coefficients are constants, calculated by least squares using values at 9 elevation angles and then spatially averaged over 5 latitudes and temporally over 9 standard profiles (Niell 1996; Qiu et al. 2020). In addition, due to the assumption of the wet MF being independent of the station height (Qu et al. 2022), the Niell model, and the corresponding VMF1 and VMF3 versions, only perform height correction on the hydrostatic delay part.

The Niell model is a linear correction model with only three parameters, a_{ht}, b_{ht}, and c_{ht}, as mentioned above. The Niell model tries to characterize the variation of MF with height at any location on the globe using only these three parameters. Its correction is very crude and rapidly deteriorates in accuracy with height. In addition, the Niell model only considers the hydrostatic part and does not model the wet part. We take wet MF into consideration, set the modeling object as MF coefficient a, and then expand the linear model to a polynomial model:

$$a_h = \sum_{i=0}^{n} \left(m_i \cdot h^i \right), \quad n = 1, 2, 3$$

(10)

Note that the Niell model is a liner model but it is not equivalent to Eq. (10) when n is equal to 1. The polynomial model is actually an approximation of the exponential model. We model the MF coefficients a_h and a_w using second- and third-order polynomials, as well as exponential models of order 1 to 3. These solutions using these different models are denoted in the following by Poly2, Poly3, Exp1, Exp2 and Exp3 respectively.

We selected a grid point (45.5° S, 82.5° W) and calculated the MF coefficients a_h and a_w for this site at a total of 54 levels of height at 200 m or 300 m intervals vertically from 0 to 14 km, and then fitted the MF coefficients using the Niell and the five solutions mentioned above. Given

atmospheric anisotropy, the MF coefficients for each height level are obtained by least squares of 7 elevation angles and averaged over 8 azimuths (same in the VMF3 strategy). The calculation is performed by ray tracing through ERA5 NWM. Figure 1 shows the results, with the upper panels depicting the fit results for a_h (left) and a_w (right) and the middle panels showing the relative residuals and the lower panels showing the slant hydrostatic delay (SHD) and slant wet delay (SWD) residuals at elevation angle 3°. It should be noted that as the coefficients a themselves are parameters with no magnitude or physical meaning, the numerical size of the residuals itself is hard to reflect the fitting effect, so we use the relative values to represent them. The relative residuals here are the difference between the model values minus the NWM values as a percentage of the NWM values. Furthermore, we found that for at altitudes above a certain value (about 6–8 km in the equatorial region and about 1–3 km in the polar regions), the variations in the wet delay MF residuals became erratic, since at these altitudes the vast majority of ZWD values were very small (< 0.1 mm) and the water vapor was already negligible. We did not use data with ZWD < 0.1 mm in the experiment because we think the precision of the reanalysis data may have reached its maximum. This problem may be solved in the future as NWM accuracy and number of layers continue to increase.

In Fig. 1, both the polynomial and exponential solutions fit well when the order is second order and above, with relative a_h residuals within ± 1% and relative a_w residuals within ± 4%. The Niell solution performs well at low altitudes as the MF coefficients are very close to linear in this region, but once the altitude is greater than 8 km, the precision of the Niell solution deteriorates rapidly, with the relative residuals of the a_h being close to 10% at 14 km altitude. The Exp1 solution performs generally better than the Niell solution, as the fit considers the entire altitude data. The Exp1 solution, like the Niell solution, features a growth in the relative a_h or a_w residuals with increasing heights, while the rest of the solutions do not show such behavior. This phenomenon of MF coefficients with heights is not reflected in the slant wet delay residuals because the water vapor gradually thins to disappear in the experimentally selected height range, causing the zenith wet delay values to become very small. From the SHD/SWD residuals, it can be found that the model precision increases with increasing order, and the residuals of the slant path delay residuals are already very close to 0 in the third-order Exp3 and Poly3 solutions. Note that since the Niell model only corrects the height for hydrostatic MF coefficient, the Niell estimate in the right panels of the figure is the result of not making any corrections.

The precision of the STD is the key indicator of the model's performance since the goal of MF height correction is to increase its precision. However, the relationship between STD precision and elevation angle is not linear, so

Fig. 1 Tropospheric delay mapping function coefficients vertical profiles (black dots) and the polynomial and exponential approximations (upper), the relative fitting residuals (middle), and the slant delay residuals at elevation angle 3° (lower). The left panels and right panels are the hydrostatic part and the wet part respectively. Note that they have different scale ranges
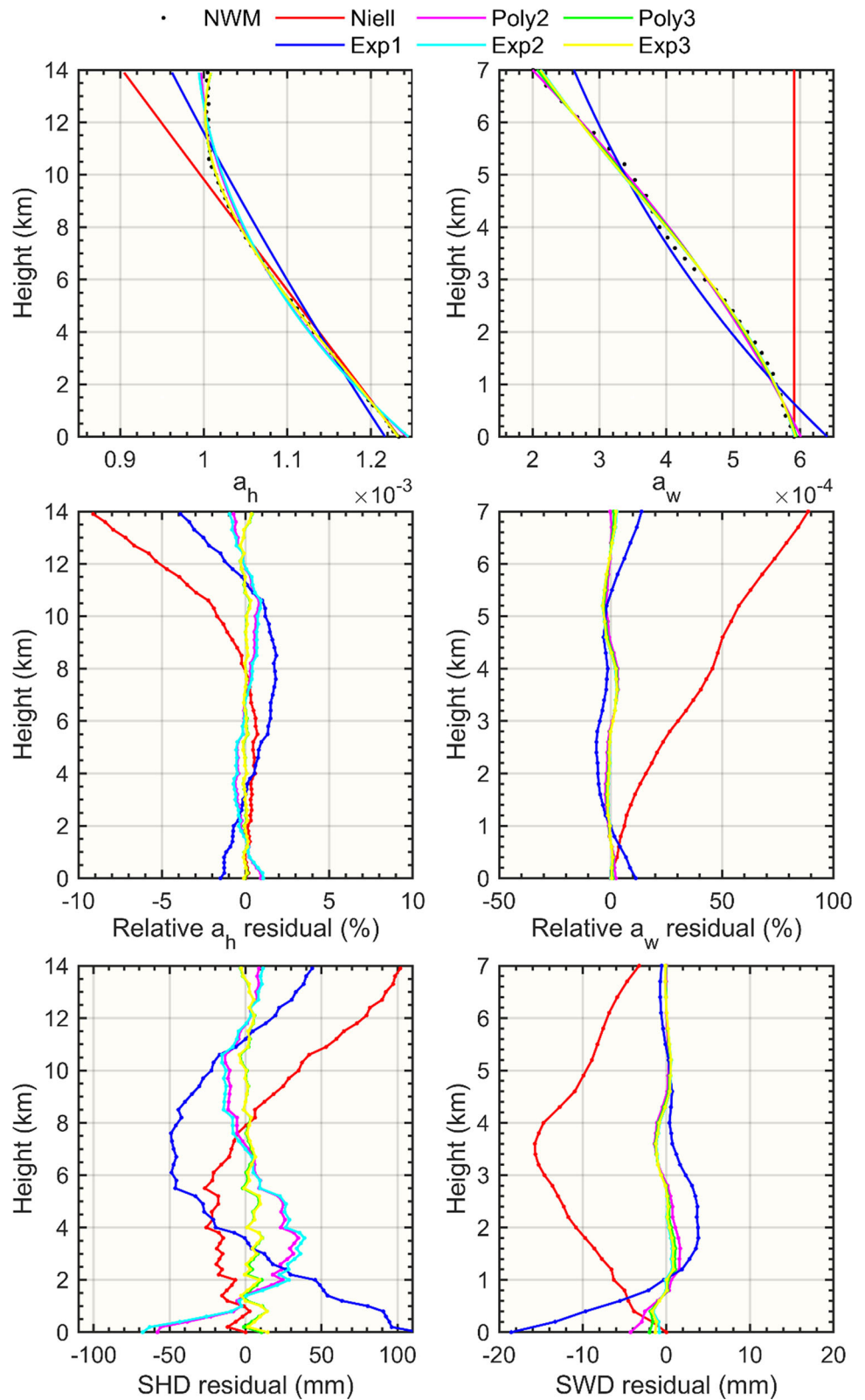
it is incomplete to select only the STD precision at a certain elevation angle for representing the model precision. Therefore, we use the relative a_h and a_w residuals directly as the evaluation metric in the next section (Another reason is that the STD precision at elevation angle 3° does not show significant spatiotemporal dependence). It should be noted that the SHD/SWD residuals in Fig. 1 are the residuals when the ERA5 ray tracing ZHD/ZWD values are used, and if using the model ZHD/ZWD values, this part of the model error will be amplified and cannot reach the precision level in Fig. 1.

3 Validating the method

In this section, we extend the experiments in Sect. 2.2 to a global 5° × 5° grid, at the first epoch of each day, at 00:00 UT of 2021, and then count the global distribution of modeling errors for the six solutions. Next, the variation of errors with latitude, altitude and time is analyzed and the precision of the polynomial and exponential models is assessed for the Earth surface using TUW's site-wise VMF1 and VMF3 GNSS products. Note that the NWM a_h or a_w in this paper is obtained by 1° × 1° ERA5 ray tracing at 8 azimuthal angles and 7 elevation angles by least squares method. The azimuth and elevation angles used and the empirical MF coefficients b and c are the same as in the VMF3. Also note that this height correction coefficients, like VMF1 and VMF3, is provided per grid point and epoch. In this study the Earth surface refers to the orography of VMF 5° × 5° grid point coordinates (based on the model ETOPO5). There are two reasons as to why we did not choose a 1° × 1° grid for this experiment. First, the number of ray calculations on a 5° × 5° grid for the current experiment is already on the order of billions, and our arithmetic power is limited. Second, and most importantly, our aim is to get high precision MFs overhead, while the size of the grid's density has little bearing on the experiment's outcomes or conclusions. The validation in this study was performed on ERA5 data, but the height correction method can also be performed on other NWMs, as there are changes in the mapping function with height that are determined by the structure of the atmosphere. Performing the calculations on other NWMs may involve values that differ from those in the present manuscript, but not to an extent that they would change the conclusions.

3.1 Modeling precision of mapping function models

To count the relative biases throughout the year and for the total altitudes, we use the relative absolute residual as an assessment indicator. It represents the modeling average precision loss and refers to the absolute value of the bias as a percentage of the ERA5 ray tracing value. The indicator is calculated as shown in Eq. (11) below, where the level refers to the height level. The results of the Niell model, Poly2 and Poly3 are shown in Fig. 2 and the results of Exp1, Exp2 and Exp3 are shown in Fig. 3. Note that we use different scales for the panels for better visualization.

$$\text{indicator} = \frac{\sum_{i=1}^{N_{\text{level}}} \left| \frac{a_{\text{model},i} - a_{era5,i}}{a_{era5,i}} \right|}{N_{\text{level}}} \times 100\% \qquad (11)$$

In the Niell and Exp1 solutions, the relative absolute residual of the a_h fitting (upper left panels of Figs. 2 and 3) shows a latitudinal dependence with notably greater values in the high latitude regions than in the low latitude regions. The relative absolute residual in the Exp1 solution is smaller than that in Niell solution, featuring the upper limits of the distribution range of 1.25% (a_h) and 4.33% (a_w) respectively. The results for the Poly2 and Exp2 solutions (middle left panels of Figs. 2 and 3) are very similar in that they both show a clear topographic effect, with the relative absolute residual of the a_h fitting being smaller at higher altitudes than at lower altitudes, and the range of values for both solutions being similar, with upper limits of 0.3% and 0.35% respectively. The Poly3 and Exp3 solutions (lower left panels of Figs. 2 and 3) are also very similar, with the upper limit of the numerical distribution dropping further to around 0.19% for both, but the topographic effect giving way to the latitudinal dependence as the Niell and Exp1 solutions. These phenomena can be attributed to the varying rates of MF decline with altitude across different latitudes. They are also associated with the fewer number of height layers present in regions of high altitude.

In comparison to the outcomes of a_h, the relative absolute residual of a_w has no more symmetry between the northern and southern hemispheres. As can be seen from the Niell solution (upper right panels of Fig. 2), without height correction, the values of residual are very large, up to twice the ERA5 ray tracing value, particularly in the middle and high latitudes of the northern hemisphere, and much bigger than in other regions. The relative a_w absolute residual is reduced to less than 5% with the Exp1 solution, despite its simplicity. The results of Poly2 and Exp3 are also very similar, with the upper limits of their numerical distributions being about 2.5% and 3% respectively. The results of Poly3 are reduced to 1.6% from that in Poly2, while in Exp3 it is reduced very little from that in Exp2, to only about 2.7%. The a_w results both show very weak topographic characteristics, with slightly smaller areas at higher elevations than at lower elevations. These characteristics in the distribution of the a_w residual reflect the sensitivity of the coefficient's precision to the water vapor content, which varies randomly with height and lacks the hydrostatic atmosphere's imprint of topography and latitude.

Fig. 2 Relative absolute residuals of mapping function coefficients a_h (left) and a_w (right) under Niell (upper), Poly2 (middle) and Poly3 (lower) solution during 2021. Note the different scales for the panels for better visualization
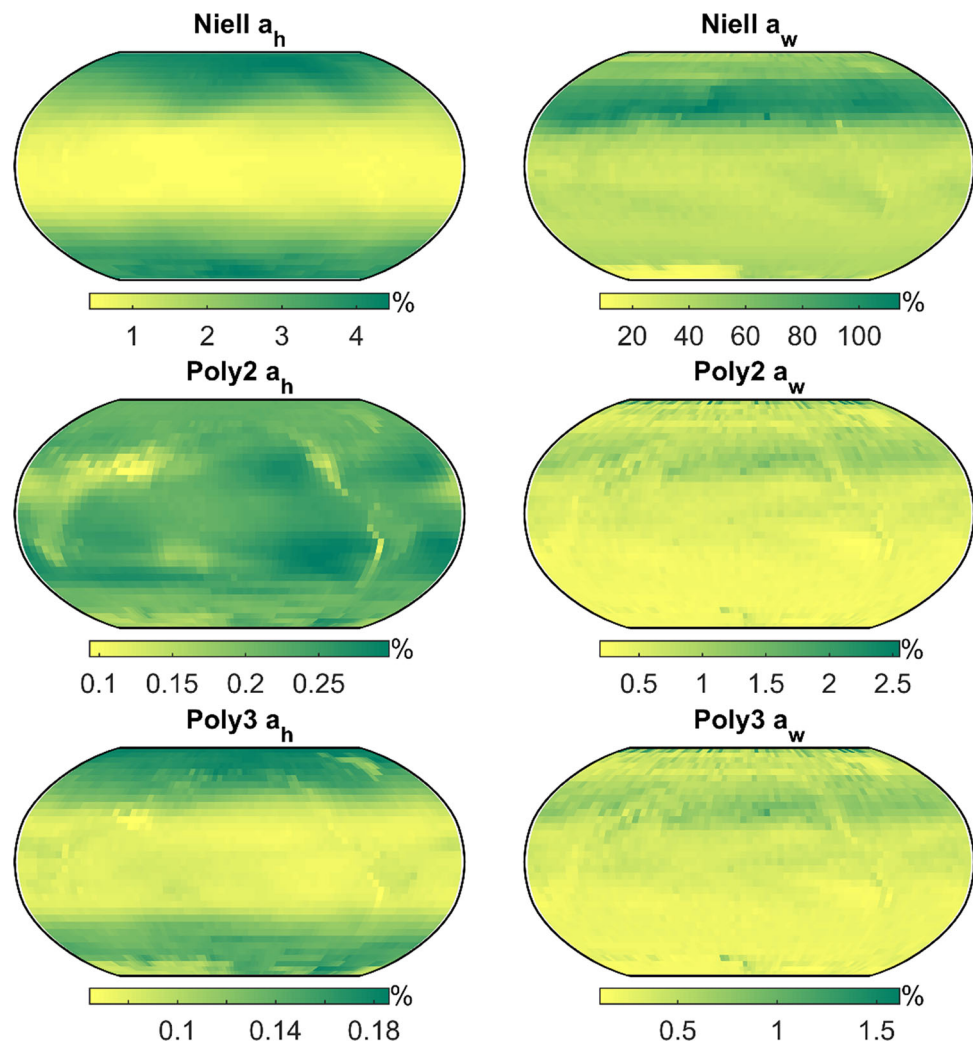
## 3.2 Modeling precision at different latitudes and altitudes

Given the results in the previous section, we have mapped the characteristics of the distribution of precision at different latitudes and altitudes more clearly. In addition, we carried out a statistical analysis by time. The mean global relative absolute residual for the six solutions were tabulated by altitude, latitude and day of years and the results are plotted in Fig. 4. As the Niell solution has a much larger residual span than the other solutions, the y-axis is broken in some panels for better visualization.

The upper panels of Fig. 4 show the altitude dependence of the modeling precision. In the Niell solution, the a_h relative absolute residual rises exponentially directly from 0% at the surface to ~ 9% at 14 km, while the a_w residual rises linearly from 0% at the surface to ~ 60% at ~ 6 km before fluctuating up and then down. The coefficient a_h precision for the Exp1 solution fluctuates within 0–2%; while, a_w precision fluctuates significantly between 6 and 10 km, and is relatively flat

at other altitudes, less than 3%. The coefficient a_h precision for the Poly2 and Exp2 solutions varies very little between altitudes, both fluctuating between 0 and 0.5%. In contrast, the Poly3 and Exp3 solutions a_h precision showed little difference, both fluctuating between 0 and 0.2%. In addition, there is almost no difference in the a_w precision of the Poly2, Poly3, Exp2, Exp3 solutions, and it is barely noticeable that the 3rd order model is more accurate than the 2nd order.

The middle panels of Fig. 4 show the latitude dependence of the modeling precision. For a_h, the Niell solution and the Exp1 solution are similar in that they both exhibit a 'U' shape, i.e., precision decreases with increasing latitude; Niell solutions precision is approximately 0.5% at equatorial regions and 4% at high latitudes; while, the two values for the Exp1 solution are approximately 0.3% and 1.2% respectively. Poly2 and Exp2 precision are very similar across latitudes, and Poly3 and Exp3 precision are also very similar across latitudes, with no significant latitudinal correlation for any of the four solutions. The two second-order solutions have precision of approximately 0.3% and the two third-order solutions

Fig. 3 Relative absolute residuals of mapping function coefficients a_h (left) and a_w (right) under Exp1 (upper), Exp2 (middle) and Exp3 (lower) solution during 2021. Note the different scales for the panels for better visualization
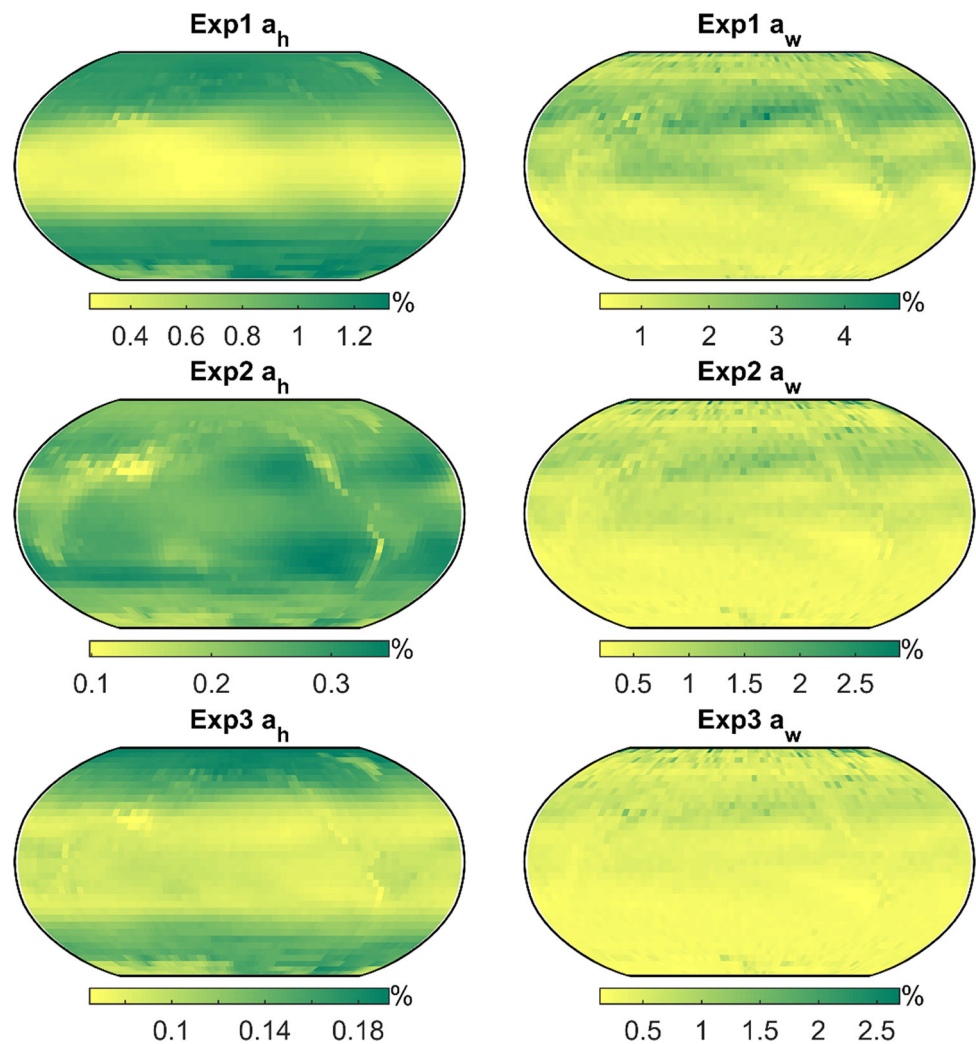
are less than 0.1% at most latitudes. For a_w, the Niell solution precision rises from about 20% at 90° S to about 40% at 60° S, remains largely at about 40% between 60° S and 30° N, then rises to about 100% between 30° N and 45° N, and finally drops to 50% between 45° N and 90° N. The latitude dependence is weak for the remaining five solutions of a_w, with the Exp1 solution being slightly more correlated than the others.

The lower panels of Fig. 4 are divided into northern hemisphere and southern hemisphere two parts to show the time dependence of the modeling precision. The a_h precision of the different solutions did not differ markedly between the northern and southern hemispheres. The a_h precision of the Niell solution had a seasonal pattern, which was higher in summer than in winter in the northern hemisphere and higher in winter than in summer in the southern hemisphere. However, the other five solutions had no significant seasonal pattern. From the performance of relative residuals in the northern and southern hemispheres, the a_w precision of different solutions has significant seasonal pattern in

the northern Hemisphere, with Niell solution having higher summer precision than winter, and other solutions having lower summer precision than winter precision. In the southern hemisphere, only the a_w precision of the Niell solution showed significant seasonal characteristics, with the same pattern as in the northern Hemisphere, with higher summer precision than winter precision. In addition, both a_h and a_w precision of the 5 solutions proposed in this paper are very stable throughout the year, and the higher the order, the better the precision. The relative absolute residuals of a_h at the first, second and third orders are about 0.8%, 0.2% and 0.1% respectively, and the relative absolute residuals of a_w at the first, second and third orders are about 1%, 0.4% and 0.25% respectively. Overall, these evaluations suggest that the newly introduced method exhibits both spatial and temporal stability. This further implies that there is no immediate need for higher grid resolution and temporal resolution.

To investigate whether our modeling method has sufficient fidelity also in other years, we selected the data on the first day of every month for a total of 10 years from 2012 to

Fig. 4 Modeling precision of hydrostatic MF coefficient a_h (left) and wet MF coefficient a_w (right) using 6 solutions at different altitudes, different latitudes and different day of year of 2021 (Northern hemisphere and southern hemisphere). The vertical black dotted line and the vertical black solid line are the dates of the summer and winter solstices, respectively
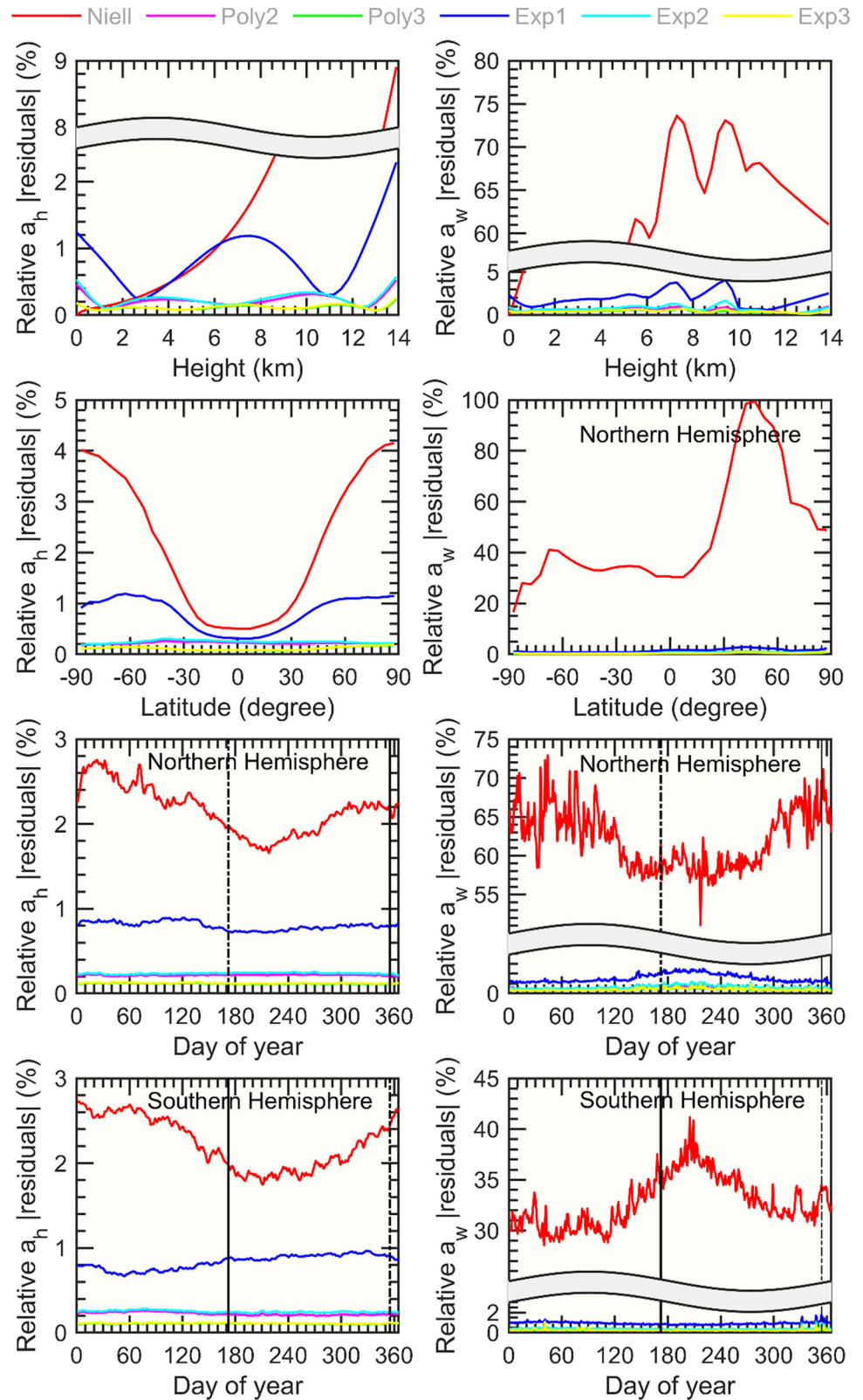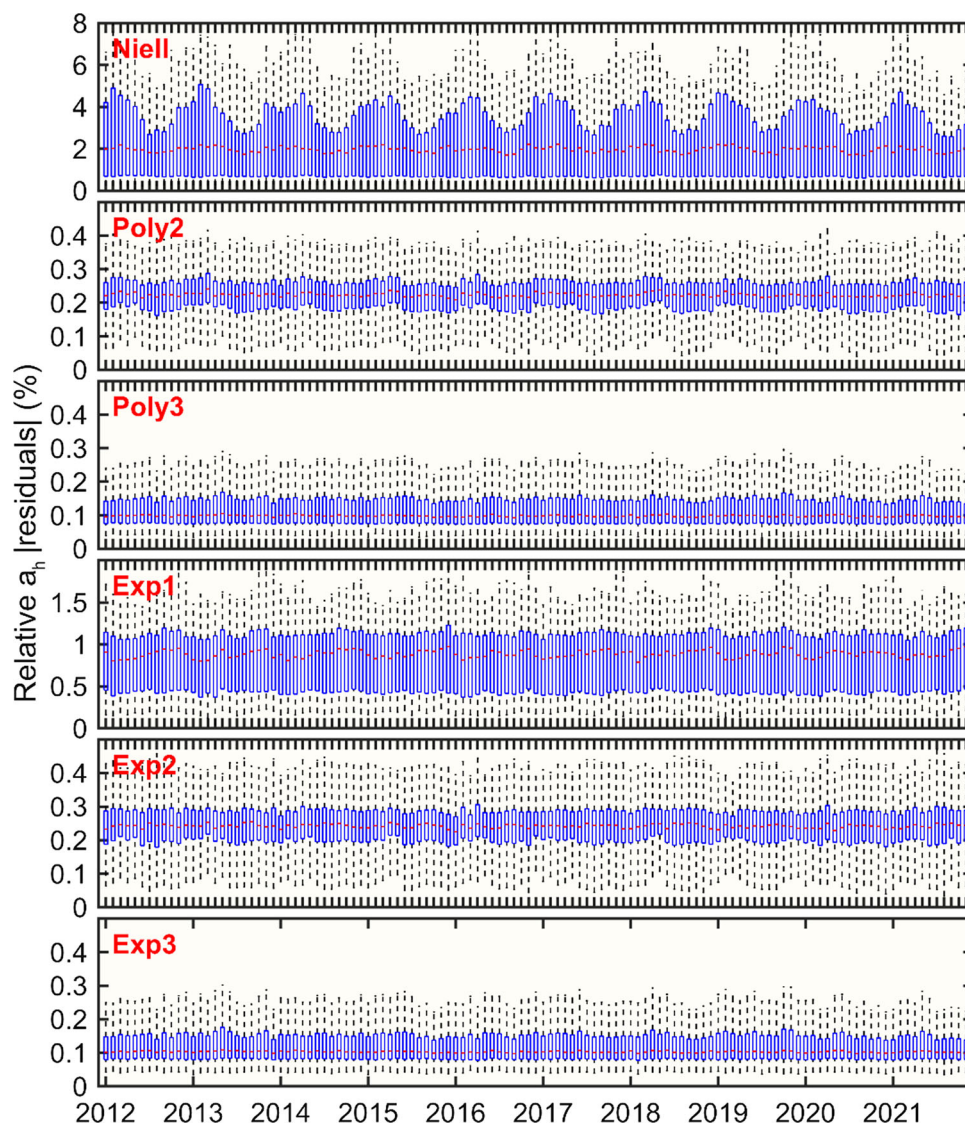
Fig. 5 Model precision of
hydrostatic MF coefficient a_h
using 6 solutions at year of
2012–2021. Each box in the
boxplot diagram represents the
result of an epoch. Note that the
first-order Niell and Exp1 scales
are larger than others

2021 to model the MF coefficients a_h and a_w vertically, and obtained the modeling precision of the hydrostatic MF coefficient a_h (Fig. 5) and the wet MF coefficient a_w (Fig. 6) under six solutions. Figures 5 and 6 are both box plots, with the red point being the median, and the top of the black dashed line, the top of the blue bar, the bottom of the blue bar, and the bottom of the black dashed line, being the upper limit, the upper quartile, the lower quartile, and the lower limit, respectively.

Figures 5 and 6 show that the model precision is fairly consistent across years with no discernible inter-annual variations. This suggests that the models put forth in this work are appropriate for modeling longer time series of data. Figure 5 demonstrates that the Niell solutions has a significant periodic signal in the model precision, whereas the other solutions do not. This further demonstrates that the method proposed in this paper can effectively simulate the seasonal

variations in the vertical profiles of the coefficient a_h. While the results for the coefficient a_w under the various solutions (Fig. 6) are not as substantial as those for the coefficient a_h, it is nevertheless evident that as the model order rises, both the median of model precision and the amplitude of the periodic signal are diminished.

In the preceding analysis, comparison of a_h or a_w relative residuals shed light on modeling effects between different models and the spatial–temporal correlation characteristics of the modeling residuals. However, a more intuitive depiction of the modeling effect would be desirable. Therefore, we counted the root-mean-square errors (RMSE) of different models at an elevation angle of 3° and plotted them in Fig. 7. Note that the RMSE here uses the slant tropospheric delay of the ERA5 ray tracing at an elevation angle of 3° as a reference. In Fig. 7, the blue error bar represents the standard deviation of the time series of the global mean of the

Fig. 6 Model precision of wet MF coefficient a_w using 6 solutions at year of 2012–2021. Each box in the boxplot diagram represents the result of an epoch. Note that the first-order Niell and Exp1 scales are larger than others
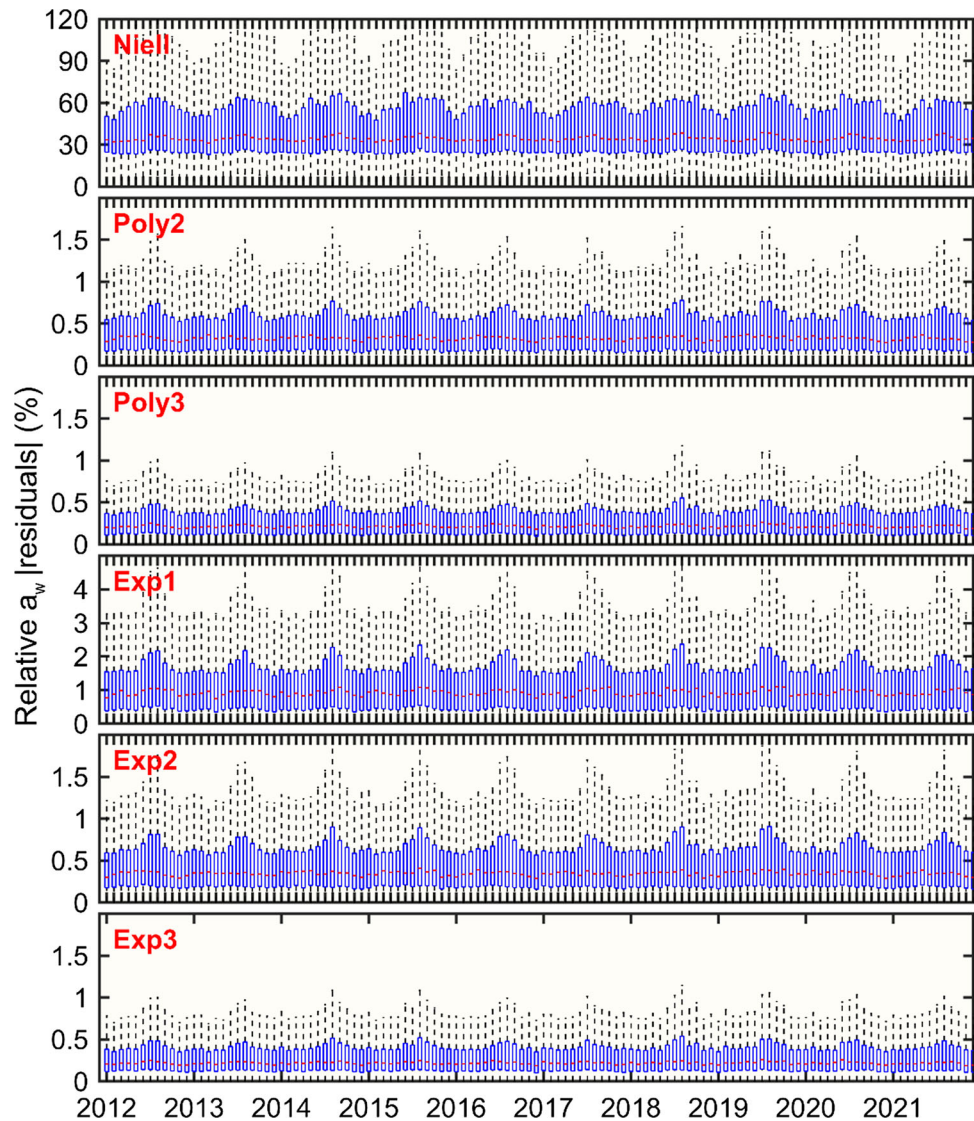
RMSE. Evidently, the difference in the RMSE of the slant tropospheric delay between the different solutions is not as significant as the difference in the relative residuals between the different solutions. There are two reasons for that. First, the statistics in Fig. 7 represent average results of global and all height levels, and second, the zenith delay becomes smaller in the high-altitude region, such that the large a_h or a_w residuals do not show up as large SHD/SWD residuals. It is important to note that this result is based on the accurate zenith delay. Such high precision cannot be achieved if the zenith delay is obtained using an empirical model.

3.3 Modeling precision with site-wise VMF1 and VMF3

In Sects. 3.1 and 3.2, we have presented an internal precision validation. To obtain external precision validation for

the new method, it is necessary to introduce external data to evaluate the model. As there are no overhead vertical MF tropospheric delay products available, it cannot be evaluated in the full vertical plane currently. To facilitate comparisons with existing studies and to further guarantee the precision of the experiment, the site-wise GNSS VMF1 and VMF3 products from TUW were used to assess the precision of the new model at ground level. The method of calculating the a_h and a_w of GNSS site locations using the new models is the same as that of the VMF3, i.e., the four nearest grid points to the site are first obtained, then the MF coefficients of the four grid points at the site height are calculated by the new models, and finally the coefficients are interpolated to the site locations. Since there are no GNSS stations with latitude greater than 87.5°N and 87.5°S in this paper, nearest neighbor interpolation is not used, but bilinear interpolation is favored. The Niell model is not discussed here as it relies on ground
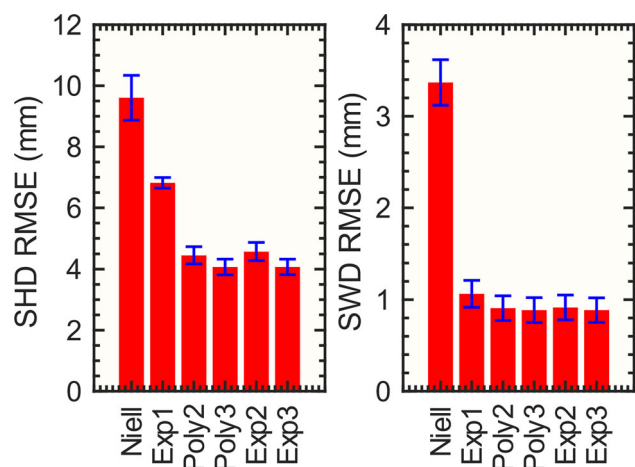
Fig. 7 RMSE of slant hydrostatic delay (left) and slant wet delay (right) using 6 solutions at elevation angle 3° of 2021. The blue error bar in the figure is the standard deviation of the corresponding model throughout the year

data and is a ground-based model. The evaluation results for each site are shown in Fig. 8 (VMF1) and Fig. 9 (VMF3), and the statistical results are shown in Fig. 8. To facilitate comparison with previous studies, we use the RMSE of the slant delay at an elevation angle of 3° as a precision indicator. Note that NWM differences can also introduce differences in results on the millimeter level (Nikolaidou et al. 2018). To concentrate on the performance of the MF height correction models and to minimize the influence of other factors, a consistent approach was adopted in our comparisons. When the VMF1 product was used as a reference, all zenith delays were derived from the VMF1 product. When the VMF3 product was used as a reference, all zenith delays were obtained from the VMF3 product.

In the evaluation of the coefficient a_h (left panel of Fig. 8), using the VMF1 products as reference, the Exp1 solution of a_h has the worst precision, especially in the mid to high latitudes of the northern hemisphere and the high latitude regions of the southern hemisphere. The precision of a_h in other regions is very similar to those from the other four solutions. Poly2 and Exp2 solutions can be seen to be slightly less accurate than Poly3 and Exp3 solutions, mainly in the west coast of South America and throughout North America. For the coefficient a_w (right panel of Fig. 8), there is no significant difference between the five solutions, and the stations with poorer precision are mainly located in the Greenland, east-central North America, central South America and the Pacific.

The results for a_h (left panel of Fig. 9) with the VMF3 products as reference are very similar to those for a_h with the VMF1 products as reference. However, fewer stations feature poorer precision, and the 3rd order solutions Poly3 and Exp3 have better precision. The results of a_w are consistent

in distribution among different models, with overall larger values than those of VMF1 and no obvious spatial pattern. Note that despite the increased complexity in describing the wet MF compared to the hydrostatic MF, the corrected slant wet delay RMSE is actually smaller than the slant hydrostatic delay RMSE. It can be attributed to the fact that the zenith wet delay itself is only about one-tenth of the zenith hydrostatic delay.

Figure 10 shows the statistical results for the full range of stations, presented in a box plot. From the a_h results (left panel), the results with VMF1 as the reference and with VMF3 as the reference are generally consistent, with the global average RMSE for the Exp1 solution being around 150 mm; while, the remaining solutions are all less than 50 mm (the red crosses are outliers). The results for Exp1 and the two third-order solutions Poly3 and Exp3 with VMF3 as the reference are slightly more accurate than those with VMF1 as the reference. The results for a_w (right panel) show that there is no significant difference between the five solutions for either VMF1 or VMF3 as a reference. The global averages for the results with VMF1 and VMF3 as reference are around 28 mm and 48 mm for the 5 solutions. The results with VMF1 as reference are more concentrated around the mean value than the results with VMF3 as reference. Niell et al. (2001) transformed this RMSE into station height errors with a rule of thumb, i.e., "The error in the station height is approximately one third of the delay error at the lowest elevation angle included in the analysis". This factor was subsequently corrected to one-fifth by Bohm (2004). Note the above factors are given at an elevation angle of 5°, and we calculate that the slant tropospheric delay at 5° is about 0.691 times that at 3° (global scale). Therefore, translating the RMSE here into station height errors is approximately 5.5 mm for SHD and 3.5–6 mm for SWD, respectively.

4 Conclusions and perspectives

We have presented a novel method to model the tropospheric delay mapping function vertical profiles from the Earth surface up to 14 km in a simple and effective way, with a precision loss of less than 0.3% for coefficient a_h and less than 1% for coefficient a_w on the global scale. Compared to the Niell model, which was only height-corrected for a_h and had a ground data dependency, the new model adds a height correction for a_w, is not dependent on ground data and takes full account of the height variation and spatial dependency of the mapping function coefficients. The global average loss of precision for a_h and a_w decreased from 2.20 and 47.44% for the Niell model to 0.11% and 0.36% for the new model (Exp3).

Fig. 8 RMSE of slant hydrostatic delay (left) and slant wet delay (right) at elevation angle 3° using site-wise VMF1 GNSS as reference
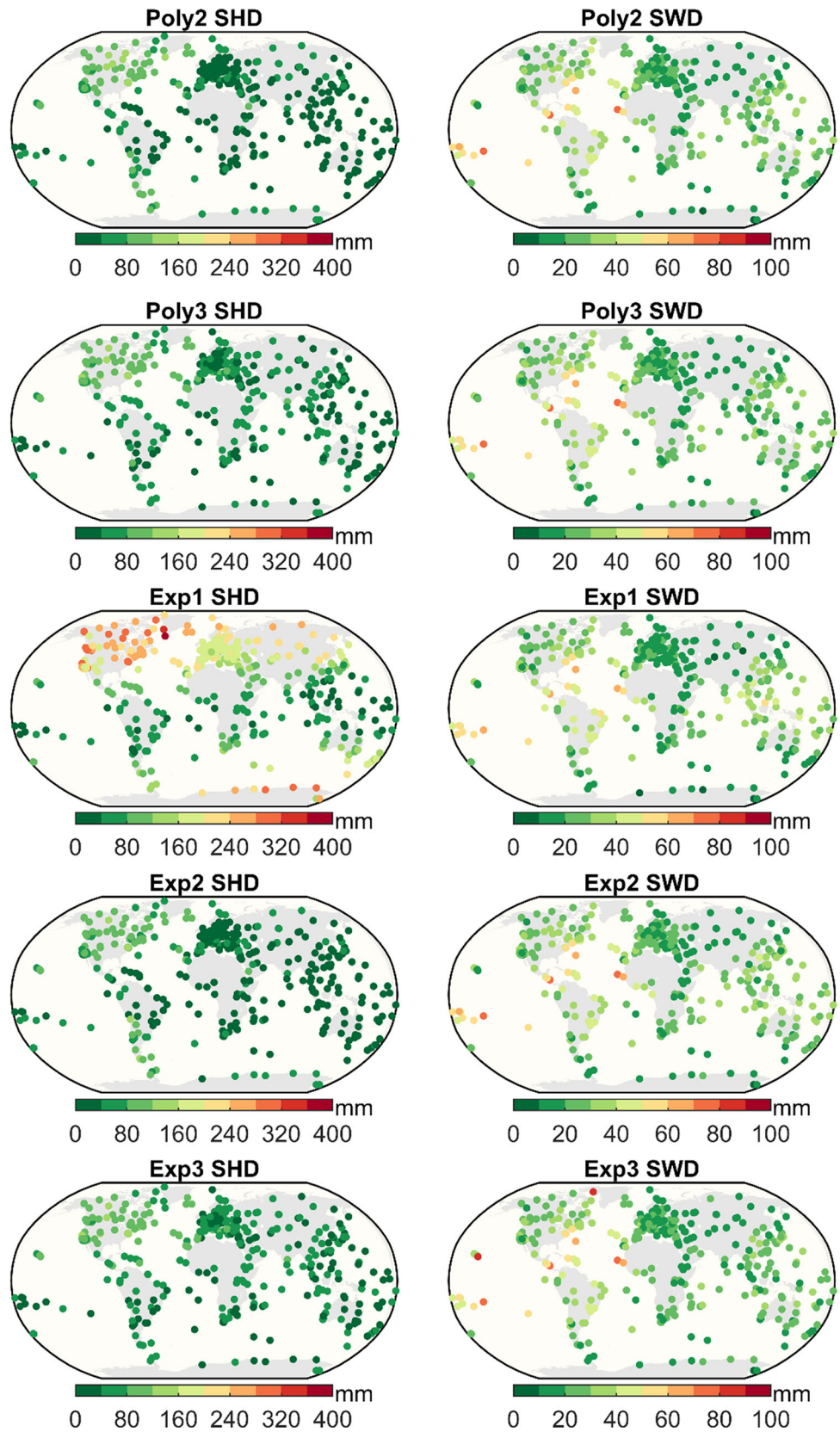
Fig. 9 RMSE of slant hydrostatic delay (left) and slant wet delay (right) at elevation angle 3° using site-wise VMF3 GNSS as reference
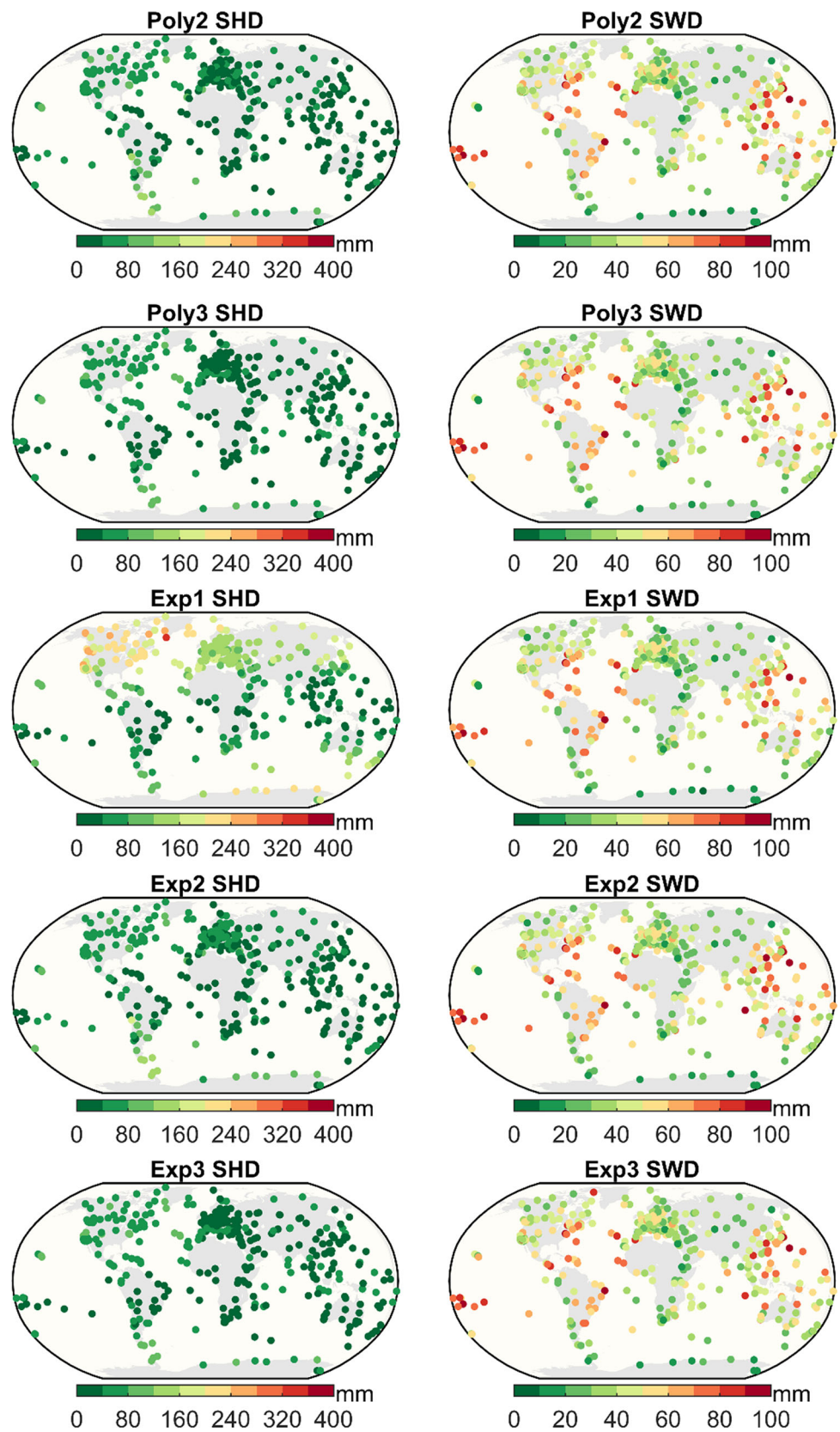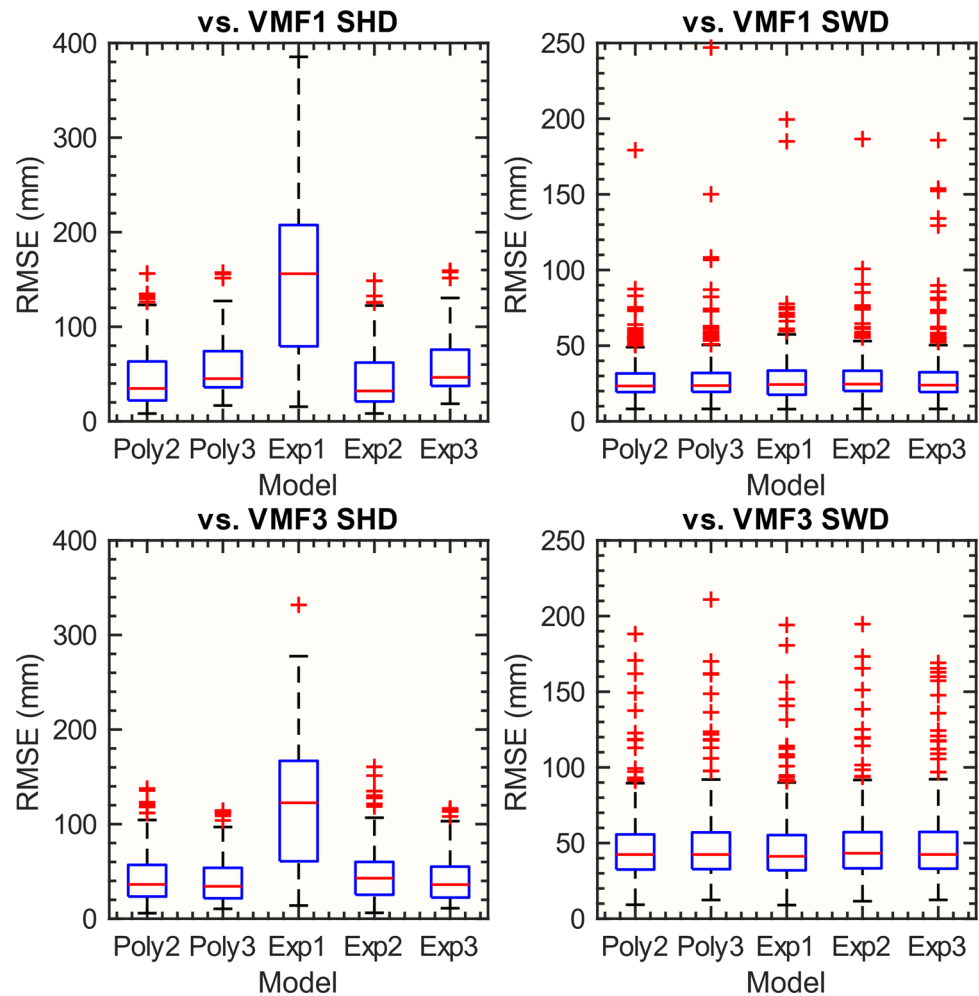
Fig. 10 Statistical results of RMSE of slant hydrostatic delay (left) and slant wet delay (right) at elevation angle 3° using site-wise VMF1 (upper) and VMF3 (lower) GNSS as reference

In our method, the vertical profile of mapping functions is represented by three to four coefficients. Given the large latitudinal dependence of the first-order model, we recommend using the second-order and higher for height correction. Third-order models can further reduce the loss of precision on top of second-order, but the improvement is limited. Using TUW site-wise VMF1 and VMF3 GNSS products as a reference, the new models also show good performance at the Earth surface, with RMSEs of about 2–5 cm for both SHD and SWD at 3° elevation angle for models of order 2 and higher.

The proposed method provides effective mapping function height correction products for the space geodesy technique community, ensuring reliable corrections from the Earth's surface to 14 km altitude (which covers the range of activities of most aircraft activities and meteorological events). The new models have no significant time dependence at second order and beyond, allowing stable precision even with empirical data. It can accommodate more users' needs, especially those who use airborne and high-altitude equipment.

Author contributions All authors contributed to the study conception and design. JC and JW proposed the idea; JD developed the software, designed the experiment and wrote the manuscript; JC, JW and YZ contributed to discussion of the idea and helped with writing. All authors reviewed the manuscript.

Declarations

Conflict of interest The authors declare no conflicts of interest.

References

Black HD (1978) An easily implemented algorithm for the tropospheric range correction. J Geophys Res Solid Earth 83(B4):1825–1828. https://doi.org/10.1029/JB083iB04p01825

Balidakis K (2019) On the development and impact of propagation delay and geophysical loading on space geodetic technique data analysis. Ph.D. Thesis, (Scientific Technical Report; 19/11), Potsdam: GFZ German Research Centre for Geosciences, pp 112–113. https://doi.org/10.2312/GFZ.b103-19114

Böhm J (2004) Troposphärische Laufzeitverzögerungen in der VLBI. Dissertation, Institut für Geodäsie und Geophysik, TU Wien, Supervisor: H. Schuh

Black HD, Eisner A (1984) Correcting satellite doppler data for tropospheric effects. J Geophys Res Atmos 89(D2):2616–2626. https://doi.org/10.1029/JD089iD02p02616

Böhm J, Schuh H (2004) Vienna mapping functions in VLBI analyses. Geophys Res Lett. https://doi.org/10.1029/2003GL018984

Böhm J, Werl B, Schuh H (2006) Troposphere mapping functions for GPS and very long baseline interferometry from European Centre for Medium-Range Weather Forecasts operational analysis data. J Geophys Res Solid Earth. https://doi.org/10.1029/2005JB003629

Böhm J, Heinkelmann R, Schuh H (2007) Short note: a global model of pressure and temperature for geodetic applications. J Geod 81:679–683. https://doi.org/10.1007/s00190-007-0135-3

Böhm J, Kouba J, Schuh H (2009) Forecast Vienna mapping functions 1 for real-time analysis of space geodetic observations. J Geod 83:397–401. https://doi.org/10.1007/s00190-008-0216-y

Balidakis K, Nilsson T, Zus F, Glaser S, Heinkelmann R, Deng Z, Schuh H (2018) Estimating integrated water vapor trends from VLBI, GPS, and numerical weather models: sensitivity to tropospheric parameterization. J Geophys Res Atmos 123(12):6356–6372. https://doi.org/10.1029/2017JD028049

Boisits J, Landskron D, Böhm J (2020) VMF3o: the Vienna mapping functions for optical frequencies. J Geod 94(6):57. https://doi.org/10.1007/s00190-020-01385-5

Chao C (1974) The tropospheric calibration model for Mariner Mars 1971. Jet Propulsion Laboratory, National Aeronautics and Space Administration, Pasadena, California, USA, Technical Report 32–1587. https://ntrs.nasa.gov/citations/19740008870

Chen J, Wang J, Wang A, Ding J, Zhang Y (2020) SHAtropE—a regional gridded ZTD model for China and the surrounding areas. Remote Sens 12(1):165. https://doi.org/10.3390/rs12010165

Ding J, Chen J (2020) Assessment of empirical troposphere model GPT3 based on NGL's global troposphere products. Sensors 20(13):3631. https://doi.org/10.3390/s20133631

Davis JL, Herring TA, Shapiro II, Rogers AEE, Elgered G (1985) Geodesy by radio interferometry: effects of atmospheric modeling errors on estimates of baseline length. Radio Sci 20(6):1593–1607. https://doi.org/10.1029/RS020i006p01593

Dousa J, Elias M (2014) An improved model for calculating tropospheric wet delay. Geophys Res Lett 41(12):4389–4397. https://doi.org/10.1002/2014gl060271

Ding J, Chen J, Tang W, Song Z (2022) Spatial–temporal variability of global GNSS-derived precipitable water vapor (1994–2020) and climate implications. Remote Sens 14(14):3493. https://doi.org/10.3390/rs14143493

Ding J, Chen J, Wang J, Zhang Y (2023) Characteristic differences in tropospheric delay between Nevada Geodetic Laboratory products and NWM ray-tracing. GPS Solut 27(1):47. https://doi.org/10.1007/s10291-022-01385-2

Foelsche U, Kirchengast G (2002) A simple "geometric" mapping function for the hydrostatic delay at radio frequencies and assessment of its performance. Geophys Res Lett 29(10):111–121. https://doi.org/10.1029/2001GL013744

Guo J, Langley RB (2003) A new tropospheric propagation delay mapping function for Elevation Angles down to 2o. In: Proceedings of the 16th international technical meeting of the satellite division of the Institute of Navigation (ION GPS/GNSS 2003) pp 368–376

Gegout P, Biancale R, Soudarin L (2011) Adaptive mapping functions to the azimuthal anisotropy of the neutral atmosphere. J Geod 85:661–677. https://doi.org/10.1007/s00190-011-0474-y

Herring TA (1992) Modeling atmospheric delays in the analysis of space geodetic data. In: Proceedirws of refraction of transatmospheric simals in geodesy, De Munck JC, Spoelstra TA (Eds), Netherlands geodetic commission publications on geodesy, vol 36, no 4

Hofmeister A (2016) Determination of path delays in the atmosphere for geodetic VLBI by means of ray-tracing. Ph.D. thesis, Department of Geodesy and Geophysics, Faculty of Mathematics and Geoinformation, Technische Universität Wien. http://resolver.obvsg.at/urn:nbn:at:at-ubtuw:1-3444

Hofmeister A, Böhm J (2017) Application of ray-traced tropospheric slant delays to geodetic VLBI analysis. J Geod 91:945–964. https://doi.org/10.1007/s00190-017-1000-7

Hersbach H, Bell B, Berrisford P, Biavati G, Horányi A, Muñoz Sabater J et al (2023) ERA5 hourly data on pressure levels from 1940 to present. Copernicus Climate Change Service (C3S) Climate Data Store (CDS). https://doi.org/10.24381/cds.bd0915c6

Kouba J (2008) Implementation and testing of the gridded Vienna Mapping Function 1 (VMF1). J Geod 82:193–205. https://doi.org/10.1007/s00190-007-0170-0

Kouba J (2009) Testing of global pressure/temperature (GPT) model and global mapping function (GMF) in GPS analyses. J Geod 83:199–208. https://doi.org/10.1007/s00190-008-0229-6

Kraus H (2001) Die Atmosphare der Erde. Eine Einfuhrung in die Meteorologie. 2nd ed. Springer-Verlag Berlin Heidelberg. 470 pp. ISBN: 3-540-41844-X

Krueger E, Schueler T, Hein GW, Martellucci A, Blarzino G (2004) Galileo tropospheric correction approaches developed within GSTB-V1. In: Proceedings of ENC-GNSS (vol 2004, pp 16–19)

Landskron D, Böhm J (2018) VMF3/GPT3: refined discrete and empirical troposphere mapping functions. J Geod 92:349–360. https://doi.org/10.1007/s00190-017-1066-2

Li W, Yuan Y, Ou J, He Y (2018) IGGtrop_SH and IGGtrop_rH: two improved empirical tropospheric delay models based on vertical reduction functions. IEEE Trans Geosci Remote Sens 56(9):5276–5288. https://doi.org/10.1109/TGRS.2018.2812850

Marini JW (1972) Correction of satellite tracking data for an arbitrary tropospheric profile. Radio Sci 7(2):223–231. https://doi.org/10.1029/RS007i002p00223

Niell AE (1996) Global mapping functions for the atmosphere delay at radio wavelengths. J Geophys Res Solid Earth 101(B2):3227–3246. https://doi.org/10.1029/95JB03048

Niell AE (2000) Improved atmospheric mapping functions for VLBI and GPS. Earth Planets Space 52:699–702. https://doi.org/10.1186/BF03352267

Niell AE, Coster AJ, Solheim FS, Mendes VB, Toor PC, Langley RB, Upham CA (2001) Comparison of measurements of atmospheric wet delay by radiosonde, water vapor radiometer, GPS, and VLBI. J Atmos Ocean Tech 18:830–850. https://doi.org/10.1175/1520-0426(2001)018%3c0830:COMOAW%3e2.0.CO;2

Nikolaidou T, Balidakis K, Nievinski FG, Santos MC, Schuh H (2018) Impact of different NWM-derived mapping functions on VLBI and

GPS analysis. Earth Planets Space 70(1):1–16. https://doi.org/10.1186/s40623-018-0865-x

Penna N, Dodson A, Chen W (2001) Assessment of EGNOS tropospheric correction model. J Navi 54(1):37–55. https://doi.org/10.1017/S0373463300001107

Qiu C, Wang X, Li Z, Zhang S, Li H, Zhang J, Yuan H (2020) The performance of different mapping functions and gradient models in the determination of slant tropospheric delay. Remote Sens 12(1):130. https://doi.org/10.3390/rs12010130

Qu X, Ding W, Teferle FN, Yuan Y, Tao T, Zhu Y, Li S (2022) Improved height correction model for hydrostatic mapping functions in GNSS data processing. J Geod 96(12):99. https://doi.org/10.1007/s00190-022-01677-y

Schüler T (2014) The TropGrid2 standard tropospheric correction model. GPS Solut 18(1):123–131. https://doi.org/10.1007/s10291-013-0316-x

Song S, Zhu W, Chen Q, Liou Y (2011) Establishment of a new tropospheric delay correction model over China area. Sci China Phys Mech 54:2271–2283. https://doi.org/10.1007/s11433-011-4530-7

Urquhart L, Nievinski FG, Santos MC (2014) Assessment of troposphere mapping functions using three-dimensional raytracing. GPS Solut 18:345–354. https://doi.org/10.1007/s10291-013-0334-8

Urquhart L, Santos M (2011) Development of a VMF1-like service at UNB. Ph.D. dissertation, Fred. Depart. of GGE, UNB, NB, CA

Vey S, Dietrich R, Fritsche M, Rülke A, Rothacher M, Steigenberger P (2006) Influence of mapping function parameters on global GPS network analyses: comparisons between NMF and IMF. Geophys Res Lett. https://doi.org/10.1029/2005GL024361

Wang J, Balidakis K, Zus F, Chang X, Ge M, Heinkelmann R, Schuh H (2022) Improving the vertical modeling of tropospheric delay. Geophys Res Lett 49(5):e2021GL096732. https://doi.org/10.1029/2021GL096732

Yuan Y, Holden L, Kealy A, Choy S, Hordyniec P (2019) Assessment of forecast Vienna mapping function 1 for real-time tropospheric delay modeling in GNSS. J Geod 93:1501–1514. https://doi.org/10.1007/s00190-019-01263-9

Zhang H, Yuan Y, Li W, Li Y, Chai Y (2016) Assessment of three tropospheric delay models (IGGtrop, EGNOS and UNB3m) based on precise point positioning in the Chinese region. Sensors 16(1):122. https://doi.org/10.3390/s16010122

Zhang D, Guo J, Fang T, Wei N, Mei W, Zhou L et al (2021) TMF: a GNSS tropospheric mapping function for the asymmetrical neutral atmosphere. Remote Sens 13(13):2568. https://doi.org/10.3390/rs13132568

Zhou Y, Lou Y, Zhang W, Bai J, Zhang Z (2021) An improved tropospheric mapping function modeling method for space geodetic techniques. J Geod 95(9):98. https://doi.org/10.1007/s00190-021-01556-y

Zhu G, Huang L, Yang Y, Li J, Zhou L, Liu L (2022) Refining the ERA5-based global model for vertical adjustment of zenith tropospheric delay. Satell Navig 3(1):27. https://doi.org/10.1186/s43020-022-00088-w

Zus F, Dick G, Dousa J, Wickert J (2015) Systematic errors of mapping functions which are based on the VMF1 concept. GPS Solut 19:277–286. https://doi.org/10.1007/s10291-014-0386-4